ARL-TR-8805 ● SEP 2019

DEVCOM ARMY RESEARCH LABORATORY

Finite Element Analysis of Geometric Effects on Ballistic Clay Backing Material

by Mary Jane Graham and Timothy G Zhang

Approved for public release; distribution is unlimited.

NOTICES

Disclaimers

The findings in this report are not to be construed as an official Department of the Army position unless so designated by other authorized documents.

Citation of manufacturer's or trade names does not constitute an official endorsement or approval of the use thereof.

Destroy this report when it is no longer needed. Do not return it to the originator.

ARL-TR-8805 ● SEP 2019

Finite Element Analysis of Geometric Effects on Ballistic Clay Backing Material

Mary Jane Graham
SURVICE Engineering Company, Belcamp, MD

Timothy G Zhang
Weapons and Materials Research Directorate, CCDC Army Research Laboratory

Approved for public release; distribution is unlimited.

REPORT DOCUMENTATION PAGE

Form Approved
OMB No. 0704-0188

Public reporting burden for this collection of information is estimated to average 1 hour per response, including the time for reviewing instructions, searching existing data sources, gathering and maintaining the data needed, and completing and reviewing the collection information. Send comments regarding this burden estimate or any other aspect of this collection of information, including suggestions for reducing the burden, to Department of Defense, Washington Headquarters Services, Directorate for Information Operations and Reports (0704-0188), 1215 Jefferson Davis Highway, Suite 1204, Arlington, VA 22202-4302. Respondents should be aware that notwithstanding any other provision of law, no person shall be subject to any penalty for failing to comply with a collection of information if it does not display a currently valid OMB control number.
PLEASE DO NOT RETURN YOUR FORM TO THE ABOVE ADDRESS.

1. REPORT DATE *(DD-MM-YYYY)*	2. REPORT TYPE	3. DATES COVERED (From - To)
September 2019	Technical Report	April–December 2018

4. TITLE AND SUBTITLE
Finite Element Analysis of Geometric Effects on Ballistic Clay Backing Material

5a. CONTRACT NUMBER

5b. GRANT NUMBER

5c. PROGRAM ELEMENT NUMBER

6. AUTHOR(S)
Mary Jane Graham and Timothy G Zhang

5d. PROJECT NUMBER

5e. TASK NUMBER

5f. WORK UNIT NUMBER

7. PERFORMING ORGANIZATION NAME(S) AND ADDRESS(ES)
CCDC Army Research Laboratory
ATTN: FCDD-RLW-PB
Aberdeen Proving Ground, MD 21005

8. PERFORMING ORGANIZATION REPORT NUMBER
ARL-TR-8805

9. SPONSORING/MONITORING AGENCY NAME(S) AND ADDRESS(ES)

10. SPONSOR/MONITOR'S ACRONYM(S)

11. SPONSOR/MONITOR'S REPORT NUMBER(S)

12. DISTRIBUTION/AVAILABILITY STATEMENT
Approved for public release; distribution is unlimited.

13. SUPPLEMENTARY NOTES
ORCID ID(s): Timothy G Zhang, 0000-0003-4440-6275.

14. ABSTRACT
Advances in X-ray imagery give clearer details into the mechanisms involved in the formation of indentation during experiments of armor packets with clay backing material. The clay backing material has traditionally been a rectangular block. Limits on the power of X-ray flashers used, however, do not allow for imagery through the clay. Therefore, targets are modified to a cylindrical shape with maximum diameter of 6 inches. This paper is a numerical investigation into the effects of target geometry on the formation of the indentation crater in the backing material for both drop testing and impact testing.

15. SUBJECT TERMS
RP#1, behind-armor blunt trauma, finite element method, depth of penetration, drop and impact testing, cylindrical geometry

16. SECURITY CLASSIFICATION OF:			17. LIMITATION OF ABSTRACT	18. NUMBER OF PAGES	19a. NAME OF RESPONSIBLE PERSON
a. REPORT	b. ABSTRACT	c. THIS PAGE			Timothy G Zhang
Unclassified	Unclassified	Unclassified	UU	43	19b. TELEPHONE NUMBER (Include area code) (410) 306-2984

Standard Form 298 (Rev. 8/98)
Prescribed by ANSI Std. Z39.18

Contents

List of Figures v

List of Tables vi

Acknowledgments vii

1. Introduction 1

1.1 Historical Background 1

1.2 Advances 3

1.3 Geometric Considerations 4

2. Numerical Study 5

2.1 Introduction 5

2.2 Computational Approach 6

2.2.1 LS-DYNA 6

2.2.2 FE Mesh and Boundary Conditions 6

2.2.3 Material Models 8

2.3 Side Impact 9

2.3.1 Depth of Penetration 9

2.3.2 Boundary Conditions 11

2.3.3 Radial Variation 13

2.3.4 Velocity Scoping Study 16

2.3.5 Clay Motion 17

2.4 Drop-Test Results 21

2.4.1 Introduction 21

2.4.2 DOP 24

2.4.3 Clay Motion 24

3. Summary and Conclusion 27

4. References 29

List of Symbols, Abbreviations, and Acronyms **32**

Distribution List **33**

List of Figures

Fig. 1 Schematic of Prather experiments and deformation time history 2
Fig. 2 Modern side-impact test 2
Fig. 3 Drop-test craters 3
Fig. 4 ARL body armor and BABT testing 4
Fig. 5 Schematic of TNO experimental set up 5
Fig. 6 Proposed cylindrical Prather-type experiments 5
Fig. 7 Rectangular and cylindrical impact-test drawings 6
Fig. 8 Overhead computational mesh at strike face 7
Fig. 9 Zhang stress–strain curve for RP#1 at 38 °C 9
Fig. 10 Time history of DOP cylinder, rectangle, and experiment 10
Fig. 11 Clay indentation, separation, and extrusion 11
Fig. 12 DOP vs. time vary the CF 12
Fig. 13 Side view of cylindrical configuration with varied CF 12
Fig. 14 Strike face of modified clay targets 14
Fig. 15 DOP change radii 14
Fig. 16 Percent and absolute difference 15
Fig. 17 Overhead rectangular and cylindrical strike face 15
Fig. 18 Time history of DOP at various impact velocities 16
Fig. 19 Maximum DOP vs. velocity of rectangular and cylindrical setup 17
Fig. 20 Velocity fields in clay for rectangular and cylindrical setup 18
Fig. 21 Pressure contours at 0.1 ms for rectangular and cylindrical setup 19
Fig. 22 Pressure contours at 0.2 ms for rectangular and cylindrical setup 19
Fig. 23 Pressure contours at 0.3 ms for rectangular and cylindrical setup 20
Fig. 24 Pressure contours at 0.5 ms for rectangular and cylindrical setup 20
Fig. 25 Schematic of rectangular and cylindrical drop test 22
Fig. 26 Overhead rectangular and cylindrical strike face 23
Fig. 27 Calculated drop-test DOP for cylinder and rectangle 24
Fig. 28 Drop-test pressure contours, both configurations 25
Fig. 29 Variations in velocity shown for drop tests, both geometries 26
Fig. 30 Variations in velocity vs. maximum DOP in drop tests, both geometries 27

List of Tables

Table 1 Material properties in impact testing 8
Table 2 Vary coefficient of friction 13
Table 3 Material properties drop testing 23

Acknowledgments

Thanks to Brian E Schuster, PhD, and Philip A Janotti, PhD, both from the Lethal Mechanisms Branch, for insightful discussion of their extensive experimental investigations of ballistic backing materials for body-armor testing.

Thanks for consultations and discussions with Daniel P Malone, PhD, on finite element modeling, meshing techniques, and state-of-the-art practices within LS-DYNA.

1. Introduction

1.1 Historical Background

The development of back face deformation (BFD) on Personal Protective Equipment (PPE) and the resultant behind-armor blunt trauma (BABT) is the foundation of a long history of exploration into the development of an appropriate surrogate material that would allow for the extrapolation of injury to the human body and the development of lightweight, unobtrusive body armor. In the early 1970s, the Law Enforcement Assistance Administration entrusted the US Army Land Warfare Laboratory to develop lightweight protective gear. The research was undertaken by the Biophysics Division of the US Army Biomedical Laboratory and others, including the US Army Natick Laboratories and Aerospace Corporation.[1]

Initial testing and evaluations of soft body armor were performed using anesthetized animal specimens, goats,[2–4] to quantify blunt-force trauma and/or broken bones. The Biophysics Division at Edgewood Arsenal was using a gelatinous material to estimate bullet lethality in the 1960s.[5] A surrogate for human tissue response evolved from goats to gelatin and, shortly thereafter, to an oily clay called Roma Plastilina No. 1 (RP#1) in the work of Prather.[6] Prather had associated the effects of BFD on a goat thorax to that of gelatin. Even though ballistic gelatin displays resistance to penetration similar to the human body, it almost completely recovers from deformation.[7] Since permanent deformation remained after impact, clay was used as backing material. Prather demonstrated a technique, measuring features of the final penetration crater, notably depth of penetration (DOP), to the probability of lethality, an expansion of Clare's analysis.[3] Figure 1 shows a historical schematic through the phases of Prather's study.

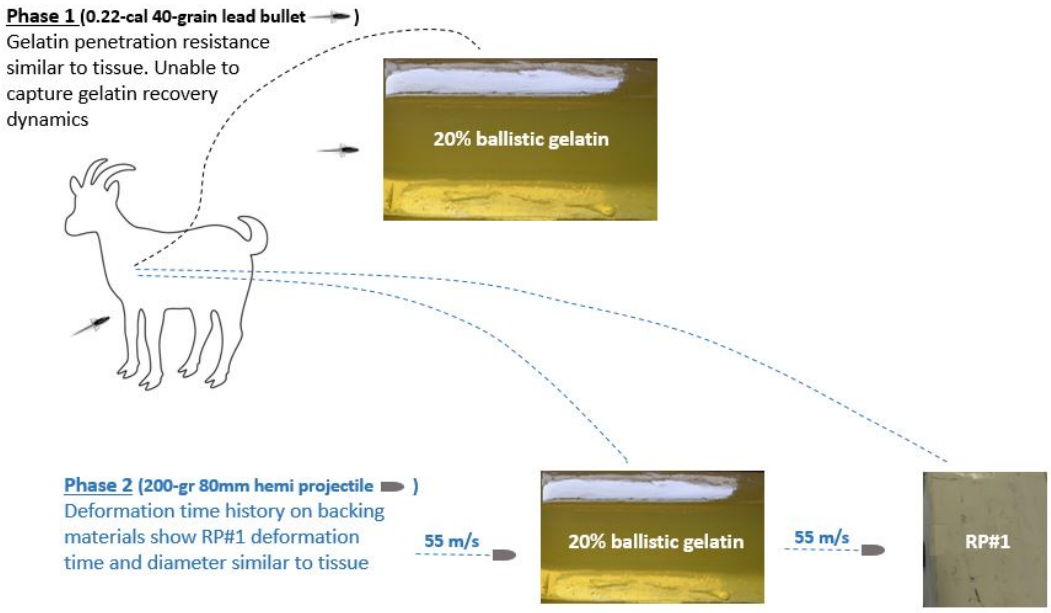

Fig. 1 Schematic of Prather experiments and deformation time history

Prather-type experiments are currently in use today to analyze BFD and BABT, to assess state-of-the-art material fabrication, and to study the effects of variation in constituent material.[8] See the images from the recent Ivancik experimental study in Fig. 2, known as side-impact tests.

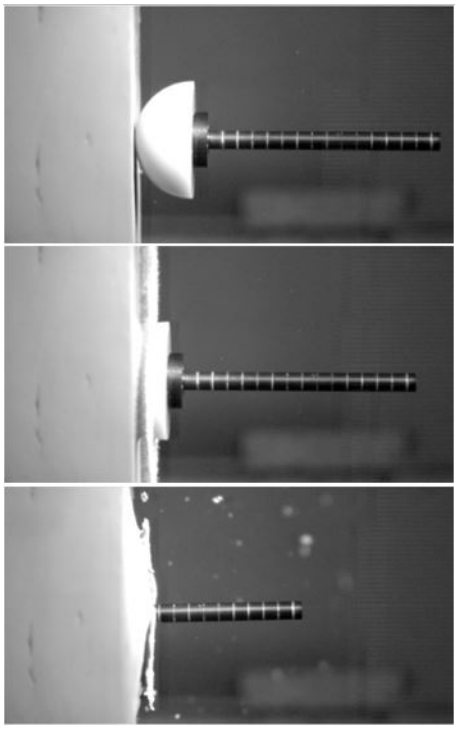

Fig. 2 Modern side-impact test

Modifications have been made to the targets of Fig. 2 to accommodate advances in diagnostic tools, such as high-speed cameras and X-ray technology. This report addresses the effects in the changes to target geometry on DOP and crater formation in RP#1 backing material.

1.2 Advances

The availability of new and emerging diagnostic tools for data collection and analysis, coupled with advances and changes made in the manufacturing of clay backing material, have resulted in modernized Prather-type experiments at Army Research Laboratory (ARL; now CCDC ARL*)[8,9] and at other agencies interested in lightweight PPE,[10,11] such as law enforcement. RP#1 is also a popular material used by various industries to model the plastic flow of metals[12–15] and for flight safety within aeronautics.[16]

The evolution of clay formulation has changed over time, giving rise to RP#1 that is temperature and time sensitive. In an attempt to quantify and manage the effect of heat treatment, and other variants, within RP#1 for body-armor testing, a column drop calibration test protocol, Test Operating Procedures (TOP), was developed at ARL[17] to examine the clay backing material for consistency prior to and after testing. Figure 3 shows an image from an ARL drop test using a spherically shaped dropper. TOP is based on the National Institute of Justice standards[18] of nonperforation and protection against blunt trauma for body armor. Other variants of drop testing have been used to characterize the dynamic response of RP#1 at medium strain rates[19] and for reference points to verify numerical studies and numerical modeling parameter-sensitivity studies.[20]

Fig. 3 Drop-test craters

* The work outlined in this report was performed while the US Army Research Laboratory (ARL) was part of the US Army Research, Development, and Engineering Command (RDECOM). As of 31 January 2019, the organization is now part of the US Army Combat Capabilities Development Command (formerly RDECOM) and is called CCDC Army Research Laboratory.

This report includes numerical modeling of drop testing on the traditional rectangular blocks of clay, similar to Fig. 3, and for the modernized cylindrical target geometry using a hemispherical dropper with cylindrical backing described in Section 2.4.1.

1.3 Geometric Considerations

Advances in X-ray imagery have provided a window into the mechanisms involved in the formation of indentation from BFD and to capture the physical features of the interaction of the experimental armor packet with the backing material. Limits on the power of X-ray flashers used today do not allow, however, for imagery through the rectangular clay blocks that have been traditionally used.[6,8] The modified target is a cylinder of RP#1 confined in a stiff material, usually polyvinyl chloride (PVC) with maximum diameter of the PVC is 6 inches (Fig. 4).

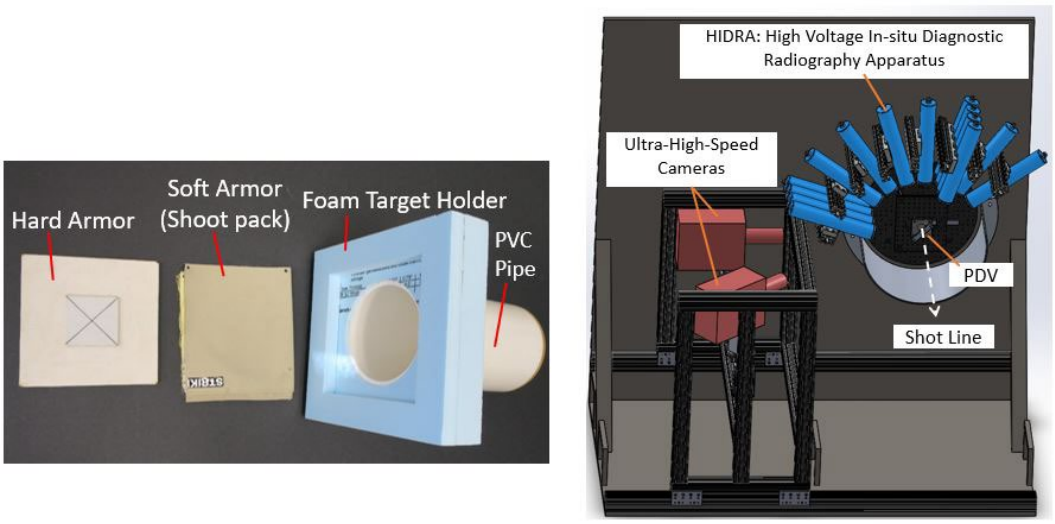

Fig. 4 ARL body armor and BABT testing

ARL performed a series of body-armor testing with state-of-the-art diagnostics, High Voltage In-situ Diagnostic Radiography Apparatus (HIDRA), to capture the dynamic BFD of the armor and penetration into the backing material.[9] Experimental observations show that the dynamics of the DOP within cylindrical geometry are different from impact experiments on rectangular blocks of RP#1. Figure 4 shows schematic of HIDRA experiments and target.

The Netherlands Organization for Applied Scientific Research (commonly known as TNO) performed experiments to study the assertion that the indentation into the clay is a complete imprint of the BFD.[10] TNO reported, however, that separation occurs between the armor and the clay, and it found some rebound within the clay. A schematic of the TNO experimental set up is shown in Fig. 5.

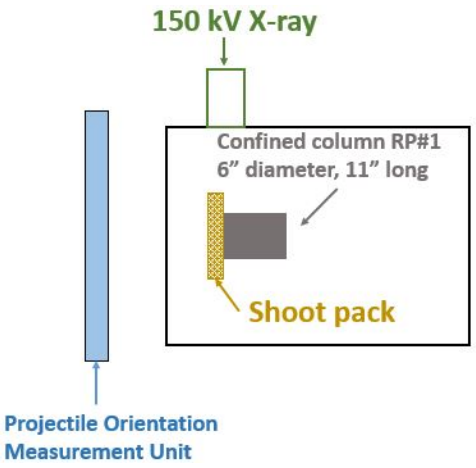

Fig. 5 Schematic of TNO experimental set up

Modernized Prather-type experiments are planned at ARL to address the geometric effects on BABT phenomena. All cylindrical impact tests will be performed without a shoot pack. See Fig. 6 for proposed cylindrical target configuration. This report is a numerical investigation into the effects of the new geometry of BABT.

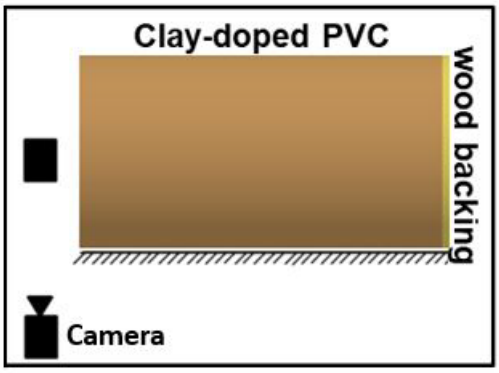

Fig. 6 Proposed cylindrical Prather-type experiments

2. Numerical Study

2.1 Introduction

The numerical studies in this paper are a continuation of the recent RP#1 finite element (FE) modeling and compression testing performed to characterize the material response of ballistic RP#1 by Zhang.[21] The work included FE modeling of Prather-type impact tests in rectangular geometry[21] using a clay-material model designed from compression tests. This work uses Zhang's methodology to assess drop and impact tests in cylindrical geometry and compares the time history of the DOP and crater formation with the rectangular configuration.

2.2 Computational Approach

2.2.1 LS-DYNA

All FE computations were performed with LS-DYNA.[22] LS-DYNA is a general-purpose, multi-physics predictive capability developed by Livermore Technology Software Corporation (LTSC). LS-DYNA is available in three approaches: Lagrangian, Smoothed Particle Hydrodynamic (SPH), and Multi-Material Arbitrary Lagrangian-Eulerian (MM-ALE). While all three methodologies are appropriate for modeling soil-like material,[23] Lagrangian is chosen for this study to be consistent with the original modeling of Zhang.[21]

2.2.2 FE Mesh and Boundary Conditions

A schematic of the rectangular-clay impact tests modeled by Zhang are shown in Fig. 7 in the top left-hand side (LHS). Below the initial configuration is the proposed cylindrical target: clay-doped PVC pipe (bottom LHS, Fig. 7). The rectangular configuration is initialized to model the Prather-type experiments of Ivancik[8] discussed in Section 1.2. The rectangular block of clay has dimensions of 12 × 12 × 11 inches (304.8 × 304.8 × 279.4 mm), where 11 inches (279.4 mm) is the depth and 12 × 12 inches are the dimensions for the strike face of the clay target. The 11-inch sides are not confined. A drawing of the rectangular target is seen on the upper right-hand side (RHS) of Fig. 7.

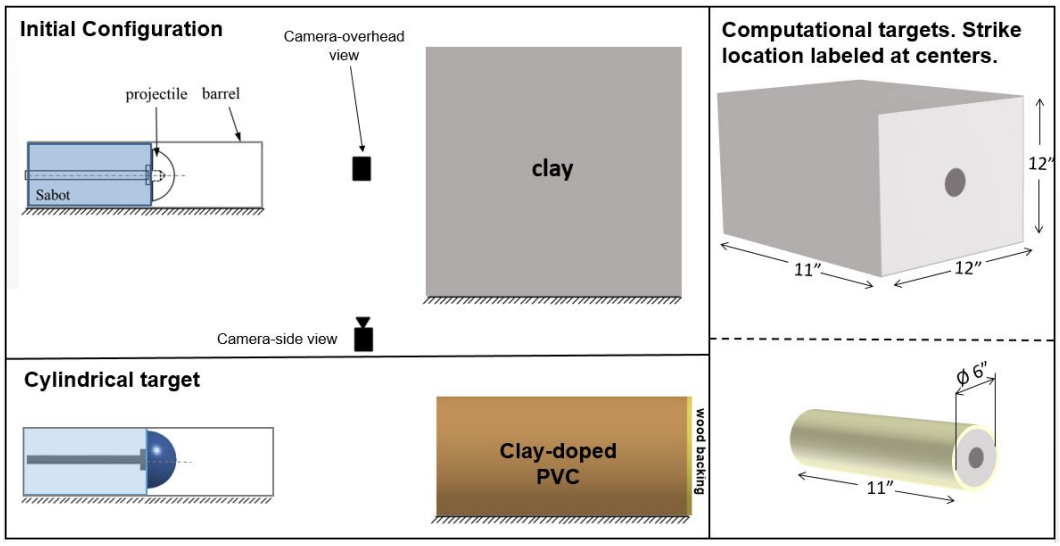

Fig. 7 Rectangular and cylindrical impact-test drawings

The projectile is a 200-g mass consisting of an 80-mm-diameter hemispherical striker with 12.4-mm tail. The striker is Nylon 101 and the tail is Delrin. The velocity of the projectile is 55.0 m/s, consistent with Ivancik's Prather-type

experimental study. The RP#1 in the cylindrical target is confined by a 6-inch (inner) diameter PVC pipe (thickness approximately 0.3 inch) with wooden backing material. The diameter of the clay is 6 inches (152.4 mm) and the length is 11 inches. The lower RHS of Fig. 7 is a drawing of the cylindrical targets with dimensions labelled.

The computational meshes for the rectangular and cylindrical geometries are shown in Fig. 8, where the cylindrical configuration has been zoomed. Symmetry planes are added in the xz- and yz-planes to reduce computational time; a quarter of the problem is modeled. These models, however, are approximations because the targets, in experiments, rest on a metal table or frame and, therefore, the symmetry is truly half. To address this issue, displacement is constrained to zero to represent the frame.[21]

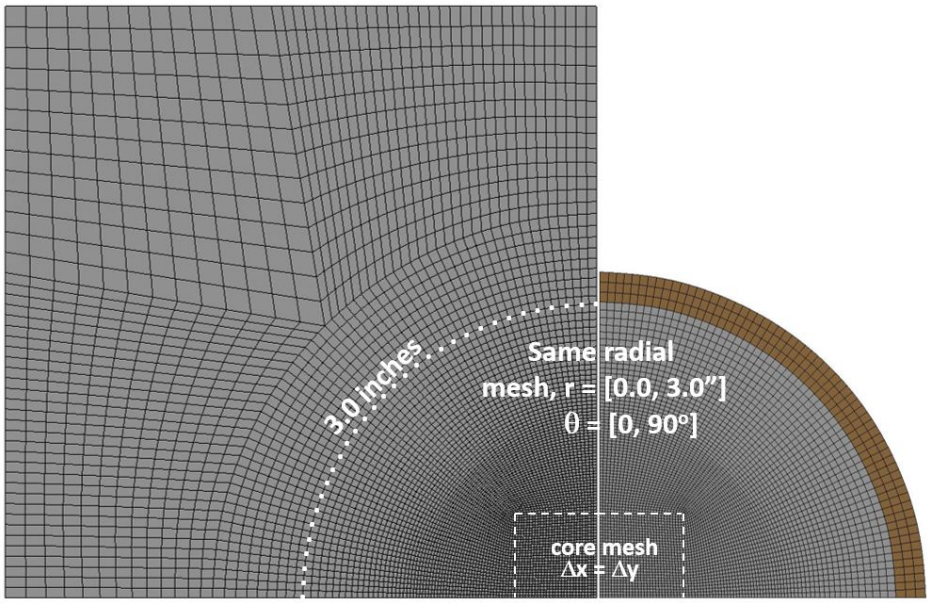

Fig. 8 Overhead computational mesh at strike face

All parts of the model (clay, projectile, PVC, and wooden backing) are partitioned into eight-node hexahedral elements, where the constant stress-element formation is used for efficiency and accuracy when severely deformed.[24] The total number of elements modeling the box configuration is 609,466, with 571,800 in the clay, and for the cylindrical setup the total number of elements is 522,826, with 418,500 in the clay.

An image of the computational mesh of the strike faces is given in Fig. 8. The clay mesh for the cylindrical configuration is the same as the inner 3.0 inches of the rectangular configuration. The core mesh, labeled with dashed lines, has the same number of elements, where $\Delta x = \Delta y$, and there is an equal number of radial zones

for radius 0.0–3.0 inches, θ from 0° to 90°. The elements in the z-direction, Δz, are the same length for both geometries.

The interface between the hemispherical part of the projectile and the clay in the impact zone is treated as an eroding surface, *CONTACT_ERODING_ SURFACE_TO_SURFACE, for both geometric configurations. The nodes at the boundary between RP#1 and PVC of the cylindrical setup are treated as a two-way contact, named *CONTACT_AUTOMATIC_SURFACE_TO_SURFACE, where penetration is not permitted from the clay into PVC and vice-versa. A sensitivity study was performed varying the coefficient of friction in the two-way contact between RP#1, 0.19, and PVC, 0.40, with results presented in Section 2.3.2. Unless otherwise stated, all numerical results for DOP were computed with coefficient of friction set to 0.19.

2.2.3 Material Models

The material properties used for the numerical investigation are listed in Table 1.[21,25,26] The material model for RP#1 is an isotropic elastic–plastic model that allows user-defined load curves for yield stress versus effective plastic strain in compression or tension and for strain-rate scaling factor on yield stress versus strain rate when material is in compression or tension, *MAT_PLASTICITY_ COMPRESSION_TENSION. The load curves are taken from the experimental and numerical study of Zhang.[21] The stress–strain curve for the RP#1 is shown in Fig. 9 at 38 °C. The curve of Fig. 9 is the baseline quasi-static material response,[21] where the compressive and tensile portions are in blue and orange, respectively. The material model used for the projectile hemisphere and rod, PVC, and wood is isotropic elastic (*MAT_ELASTIC).

Table 1 Material properties in impact testing

Property	RP#1	Projectile hemi	Projectile rod	PVC	Wood
Density (kg/m^3)	1342	1203	1485	1375	600
Young's modulus (Pa)	15.0e6	2.9e9	2.4e9	2.5e9	7.0e9
Poisson ratio	0.49	0.39	0.35	0.40	0.40

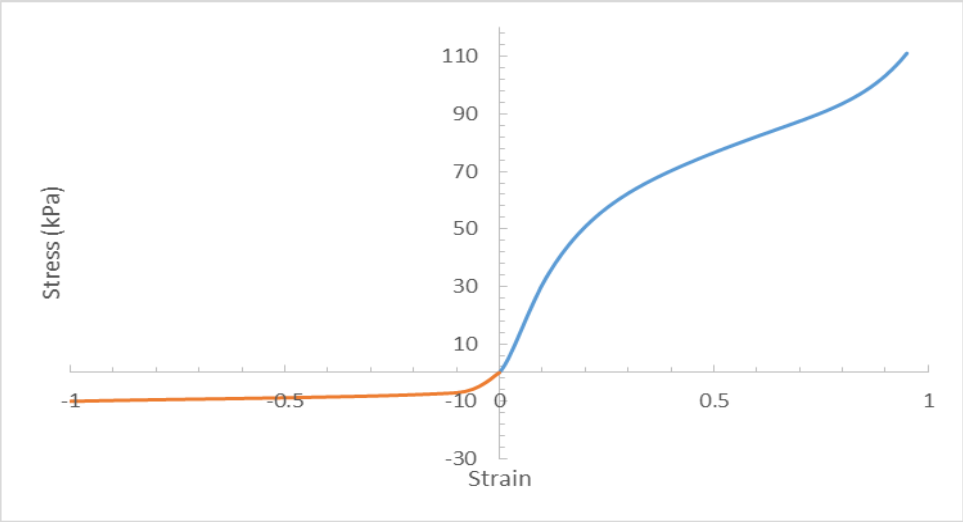

Fig. 9 Zhang stress–strain curve for RP#1 at 38 °C

2.3 Side Impact

2.3.1 Depth of Penetration

A time history of the DOP is shown in Fig. 10 for the rectangular block of clay modeled by Zhang using LS-DYNA; it is the black, solid curve. The cylindrical DOP is the green curve of Fig. 10. The minimum and maximum DOP from Ivancik's Prather-type experiments for RP#1 are the dashed red and black curves, respectively. The impact velocity for the cylinder and rectangle is 55.0 m/s, the same as the Ivancik experiments.

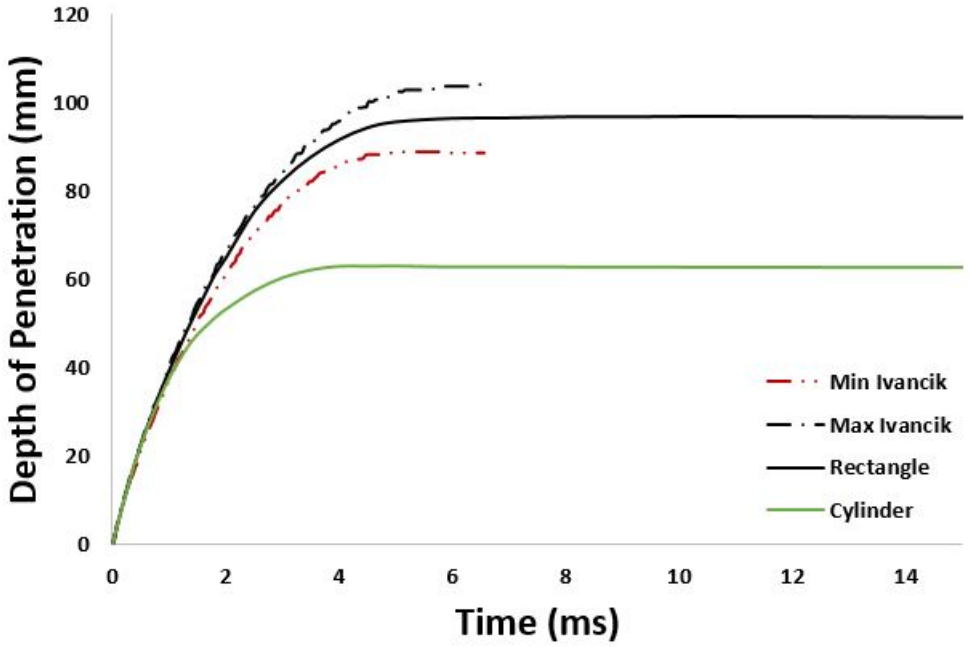

Fig. 10 Time history of DOP cylinder, rectangle, and experiment

The calculated DOP of the cylindrical target is approximately 44% less than the rectangular configuration and approximately 18% less than the minimum extracted from the Ivancik experiments (for RP#1). The decrease is caused by both reflection of pressure waves at the boundary and clay extrusion from the container. The DOP time history from Zhang's computations and the DOP time history from the Ivancik experiments are in very good agreement.

Postexperimental images of clay indentation from ARL are shown in Fig. 11. Even with armor between projectile and clay, there is clay extrusion from the PVC, between approximately 4 and 8 o'clock of the image and separation between approximately 10 and 1 o'clock.

Fig. 11 Clay indentation, separation, and extrusion

2.3.2 Boundary Conditions

Due to separation at the clay–PVC interface and extrusion from the PVC observed in the Schuster ARL experiments (shown in Fig. 11), a sensitivity study of the coefficient of friction in the boundary condition was performed.

In Fig. 12, the time history of the DOP is shown for the Ivancik experiments of RP#1, labelled minimum with red dashed curve and maximum with black dashed curve; Zhang modeling for the rectangular setup with solid black curve; and cylindrical simulations with coefficient of friction (CF) for PVC, 0.40, and for RP#1, 0.19, given by blue and green curves, respectively. The DOP for the two cylindrical cases are the same from 0.0 ms to approximately 1.9 ms. Thereafter, the DOP using the CF of the PVC at the boundary is approximately 8.0% less than when using the CF of RP#1.

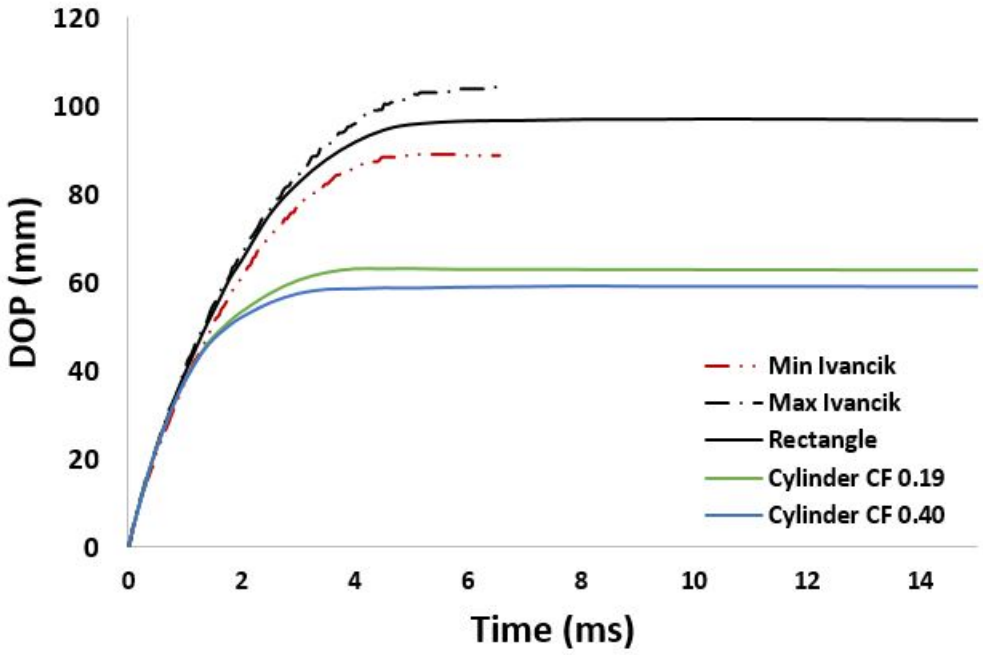

Fig. 12 DOP vs. time vary the CF

A side view of the calculations with varying CF is shown in Fig. 13. The LHS of Fig. 13 is a side view of the cylindrical calculation with the CF of the RP#1, 0.19. The RHS of the figure is using the CF of the PVC, 0.40. Each image is labeled with the maximum DOP and the amount of extruded RP#1. The maximum DOP with CF from RP#1 is 63.0 mm and occurs approximately 4.0 ms after initial impact, and the maximum DOP for the CF from the PVC is 58.6 mm approximately 3.8 ms after initial impact.

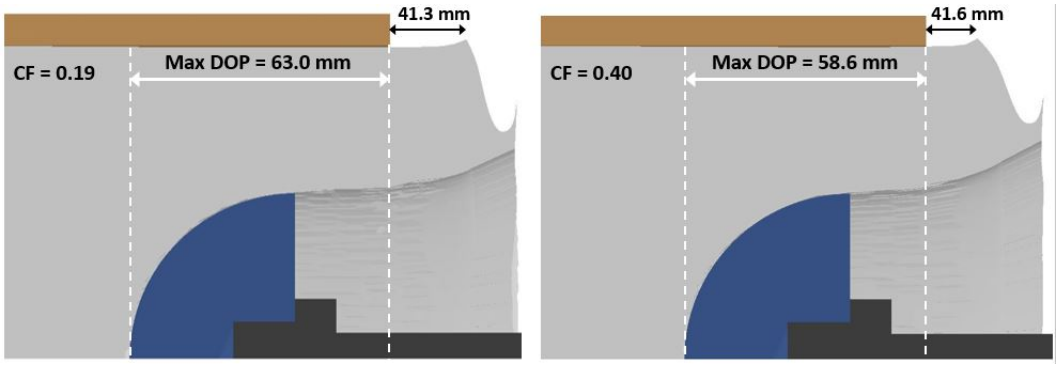

Fig. 13 Side view of cylindrical configuration with varied CF

Table 2 shows the maximum DOP, time of the maximum DOP after initial impact, and amount of extruded RP#1.

Table 2 Vary coefficient of friction

Boundary RP#1/PVC	Max DOP (mm)	Time max DOP (ms)	Extruded RP#1 (mm)
CF = 0.19	63.0	4.0	41.3
CF = 0.40	58.6	3.8	41.6

The percentage difference in the measurements of maximum DOP in Table 2 is less than 7%, which is not large given the CF of RP#1, 0.19, is less than half that of the PVC, 0.40.

The computational results reported in this study used the CF of RP#1 for consistency with the modeling of Zhang. A preliminary comparison between the cylindrical experiments performed at ARL and the amount of extruded clay indicate that the use of the CF for RP#1 is appropriate.

2.3.3 Radial Variation

The strike face of the rectangular block of RP#1 is 12 × 12 inches for consistency with the original Prather tests. The radius of the cylindrical configuration is 3 inches due to limitations on the X-ray capabilities[9,10] (as the schematic in Fig. 8 showed). The time history of the DOP for the cylindrical setup, while qualitatively the same, is lower than the rectangular setup. The time history of the DOP for each geometry should converge when 1) confining the rectangular block of clay with PVC on the outer sides and 2) increasing the radius of the clay to 6 inches, matching the distance from the center of the rectangular strike face of the clay to the outer boundary along a straight line within a plane.

The modifications to both configurations are shown, from the strike-face view, in Fig. 14. The cylindrical configuration has a plywood back end; therefore, a plywood backing, of the same thickness, was added to the rectangular setup as well. The cylindrical radius was increased from 3.0 inches to 6.0 inches to match the central dimensions of the rectangular block of clay. The rectangular block of clay is contained by PVC of the same thickness. The impactor is included in the image at the central region, where the dark blue is the hemispherical head and the black is the tail.

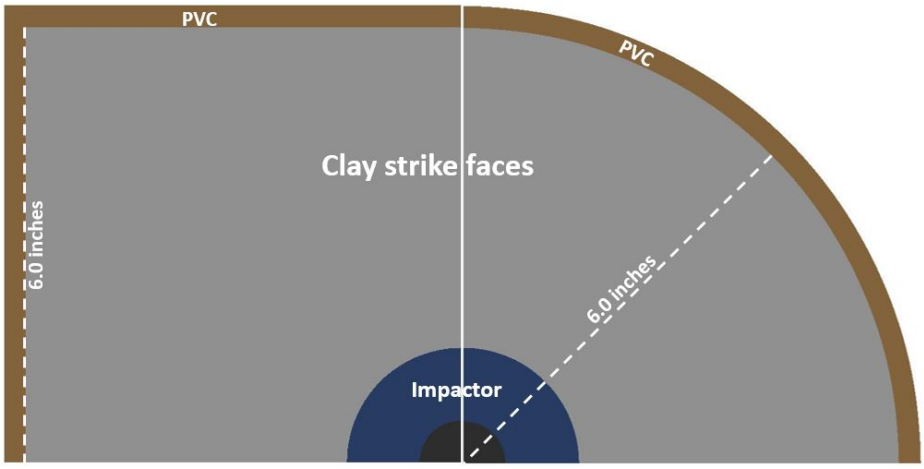

Fig. 14 Strike face of modified clay targets

The time history of the DOP for the modified targets is shown in Fig. 15. The calculation of the cylinder with increased radius to 6.0 inches, the solid-blue curve, and the rectangular configuration with PVC sides, the dashed black curve, have converged. They are qualitatively the same with the confined rectangle with plywood backing have a slightly larger DOP.

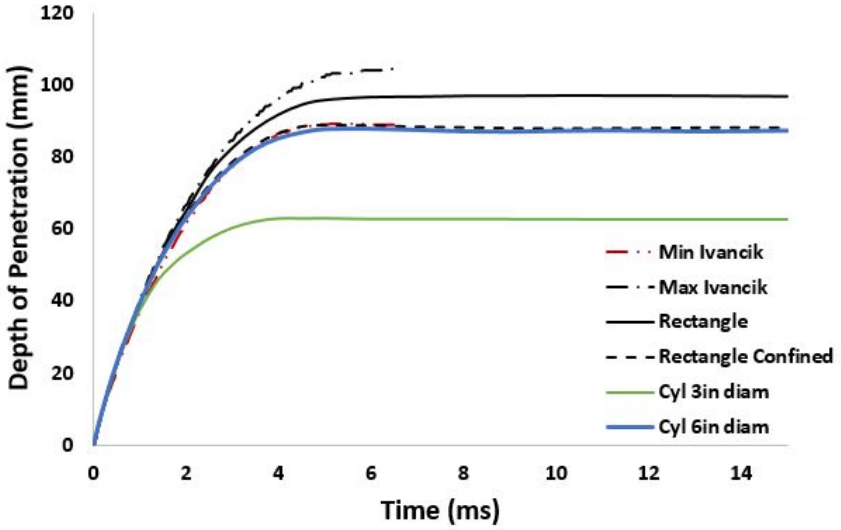

Fig. 15 DOP change radii

An overhead view of the strike-face computational mesh for the rectangular and cylindrical configurations is shown in Fig. 16. The computational mesh is the same for both configurations from the center and moving radially outward to 3.0 inches. The cylindrical geometry uses sector-shaped elements continuing to 6.0 inches. The rectangular mesh transitions from sector-shaped elements to trapezoidal from 3.9 inches to the boundaries, which may account for the minor difference in the DOP.

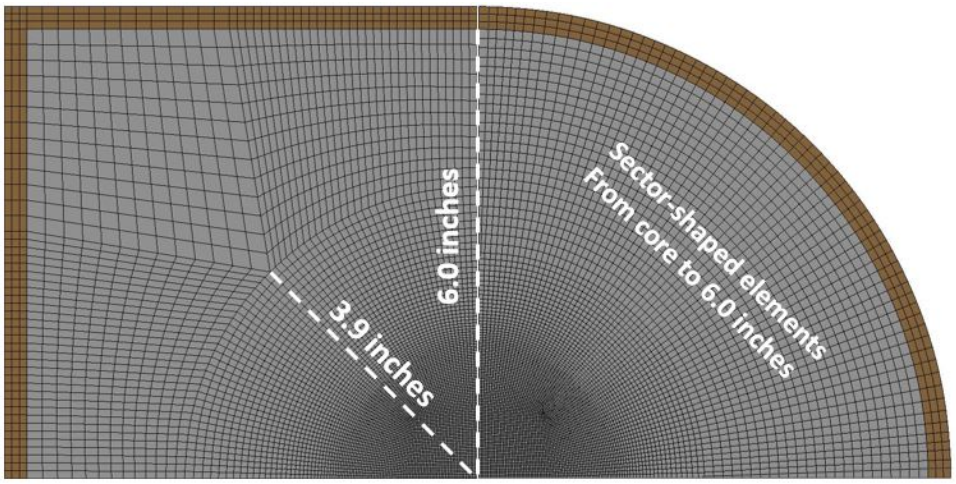

Fig. 16 Percent and absolute difference

There is a minor absolute difference in the radii of the craters between the two geometries. Figure 17 shows an overhead view of the strike faces, without penetrator, of both configurations. The LHS is the rectangular setup with PVC sides, and the RHS is the cylinder with radius increased to 6.0 inches.

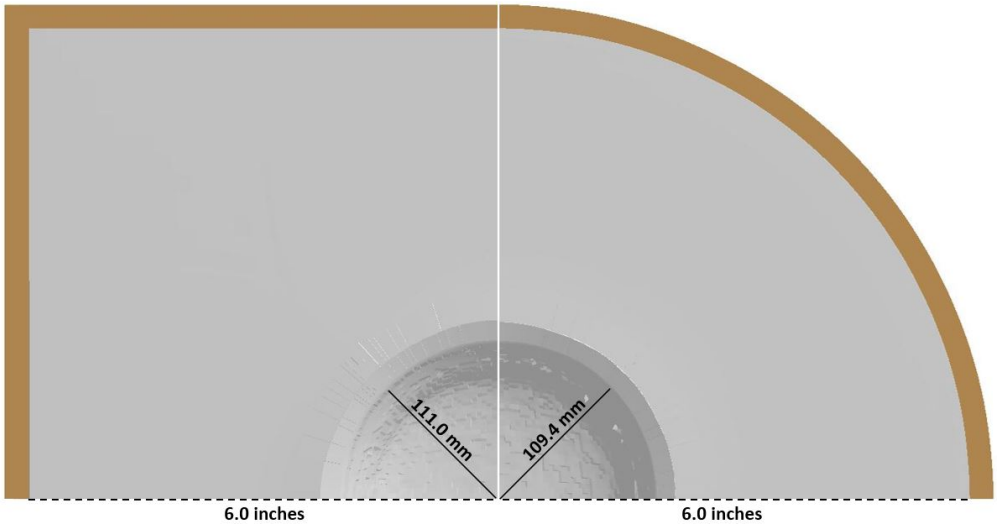

Fig. 17 Overhead rectangular and cylindrical strike face

Measurements of the crater radii were taken at 5.0 ms, the time of maximum DOP. The rectangle's crater radius is approximately 111.0 mm, and the cylinder's crater radius is 109.4 mm, which is approximately a 1.4% difference in crater radius. This is very close to the percent difference seen in the DOP of Fig. 15, which is approximately 1.2%.

2.3.4 Velocity Scoping Study

The original Prather[6] tests and the Ivancik[8] experimental study were performed at impact velocity 55.0 m/s, with some variation within the limits of reproducibility. Generally, experiments to study, analyze, and design PPE are done using hard or soft armor with clay or ballistic gelatin as a backing material. In reality, the impact velocity of threats is much higher and, therefore, the evolution of the BABT is different. In future impact experiments, the impact velocity will be increased to as high as the experimental apparatus and setup can attain, which is approximately 75.0 m/s.[27]

Time history of DOP at varying velocity was performed and is shown in Fig. 18 for both configurations, where the cylindrical impact is on the LHS in blue curves and a green curve for 55.0 m/s, and the rectangular impact is on the RHS with gray curves and a black for 55.0 m/s. The impact velocity was varied from 20.0 m/s to the anticipated maximum velocity, 75.0 m/s. The values of maximum DOP increase with velocity until stabilizing.

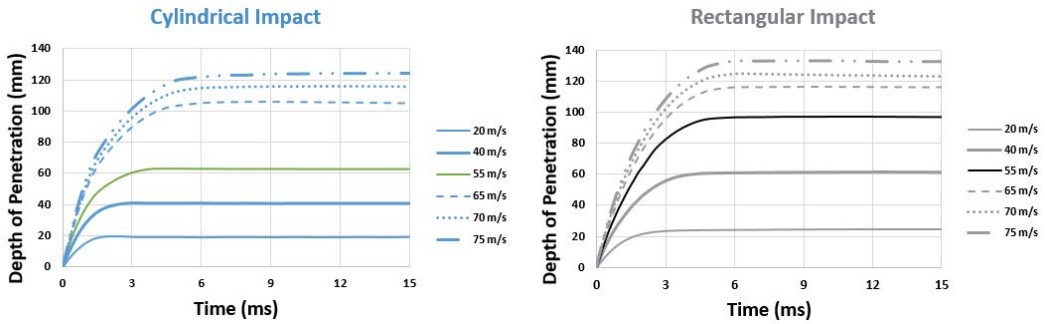

Fig. 18 Time history of DOP at various impact velocities

At the impact velocities of 55.0 m/s and higher the hemispherical impactor penetrates to a depth greater than its radius, and the clay material behind it slightly encloses the head of the penetrator, preventing rebound. Rebound was not calculated for 20.0 and 40.0 m/s for either geometry.

The graphs of Fig. 19 contain maximum DOP versus velocity. The dark-gray circular markers are for the rectangular configuration, and the blue triangular markers are for the cylindrical configuration.

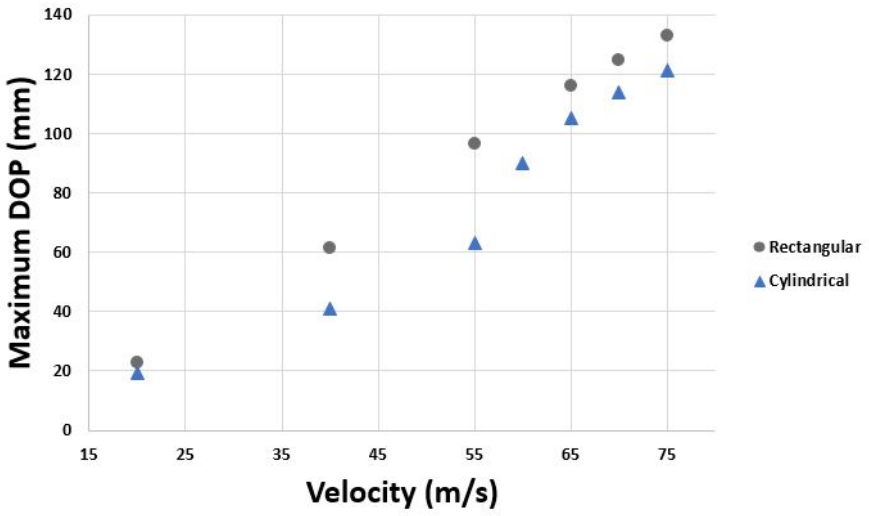

Fig. 19 Maximum DOP vs. velocity of rectangular and cylindrical setup

Maximum DOP increases at the same rate for impact velocity 60.0 m/s and higher for both configurations. The DOP for the cylindrical setup is lower than the rectangular geometry for all impact velocities.

2.3.5 Clay Motion

The time history of the DOP for rectangular and cylindrical geometry, shown in Fig. 10, is the same from 0.0 ms to approximately 0.2 ms. The pressure front, or incident waves, from the penetrator travel radially outward in the clay. The incident wave should reach the PVC approximately 0.2 ms after initial contact[28] with the clay for the cylindrical case but will continue propagating in the rectangular case.

The simulated velocity fields of the incident, as transmitted, reflected, and coalesced waves, are given in Fig. 20 at 2.0 ms. The LHS is the rectangular configuration and the RHS is the cylindrical setup. The clay of the rectangular setup of Fig. 20 has been cropped approximately 1.5 inches, but the simulation was performed for the full 6.0 inches from the center of the block. The white dashed line in the clay of the rectangle marks 3.0 inches, where the PVC is located for the cylindrical setup.

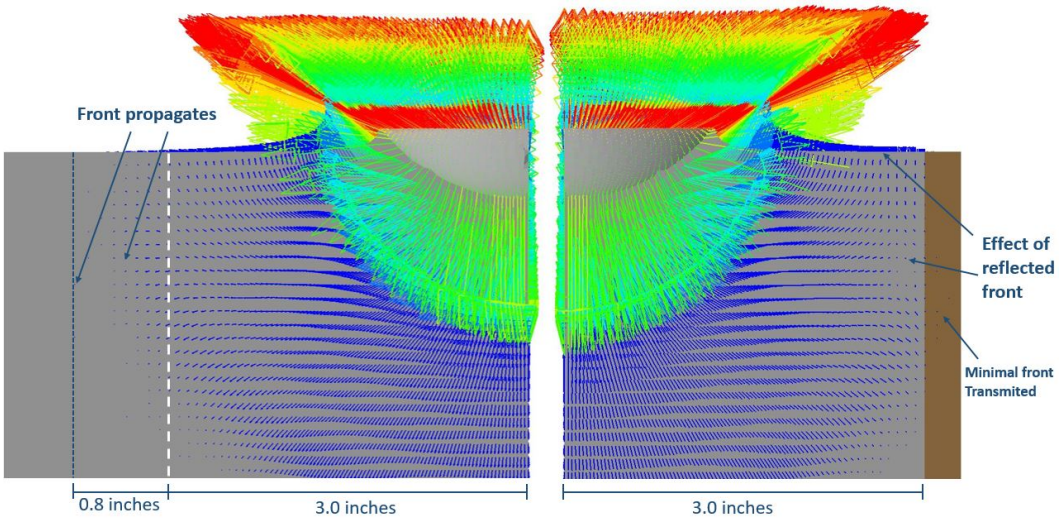

Fig. 20 Velocity fields in clay for rectangular and cylindrical setup

At 2.0 ms the incident wave of the rectangular configuration has propagated approximately 0.8 inches beyond the PVC of the cylinder. At the same time in the cylindrical configuration, the incident wave has reached the PVC, where some transmitted waves can be seen within the PVC. Most of the wave has been reflected radially inward in the clay, where the effects of coalescing waves are seen when comparing both velocity fields. At 2.0 ms, the clay of the cylindrical setup has begun the extrusion process, where the orientation and magnitude of the velocity field at the clay–PVC interface are larger.

Contours of pressure for 0.1, 0.2, 0.3, and 0.5 ms are given in Figs. 21–24, respectively. Quarter symmetry is shown with the cylindrical simulations on the top of the figures and the rectangular configuration at the bottom of the figures. The light-blue dashed lines in the cylindrical images are the location of the PVC boundary. The clay block is not confined for impact simulations. The cylindrical contours do not include the wood backing, although they were calculated with it. Therefore, the length of the targets in Figs. 21–24 is 11 inches of clay for both geometries.

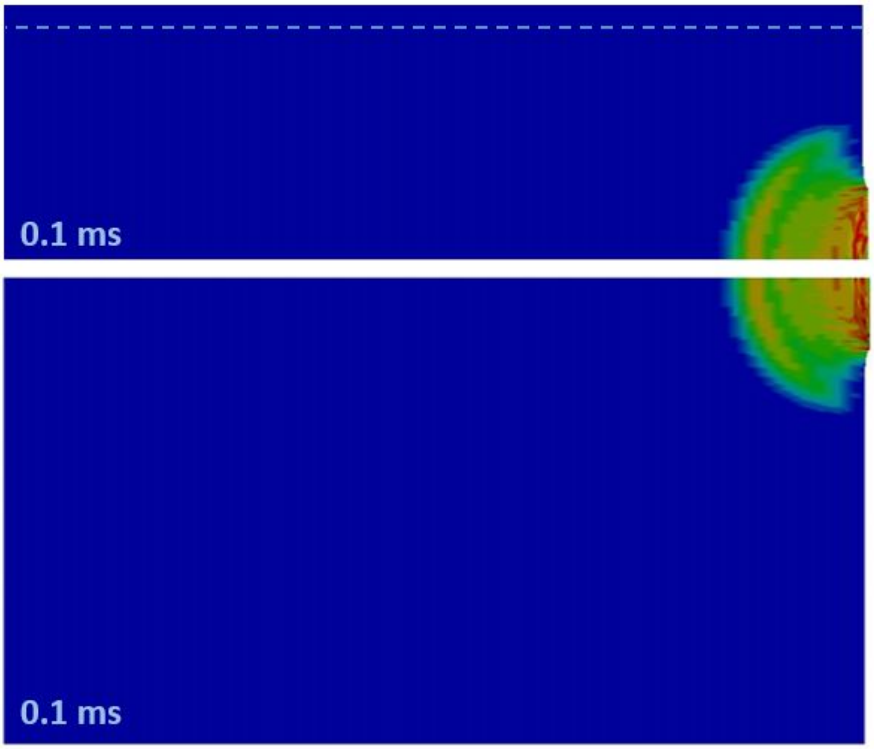

Fig. 21 Pressure contours at 0.1 ms for rectangular and cylindrical setup

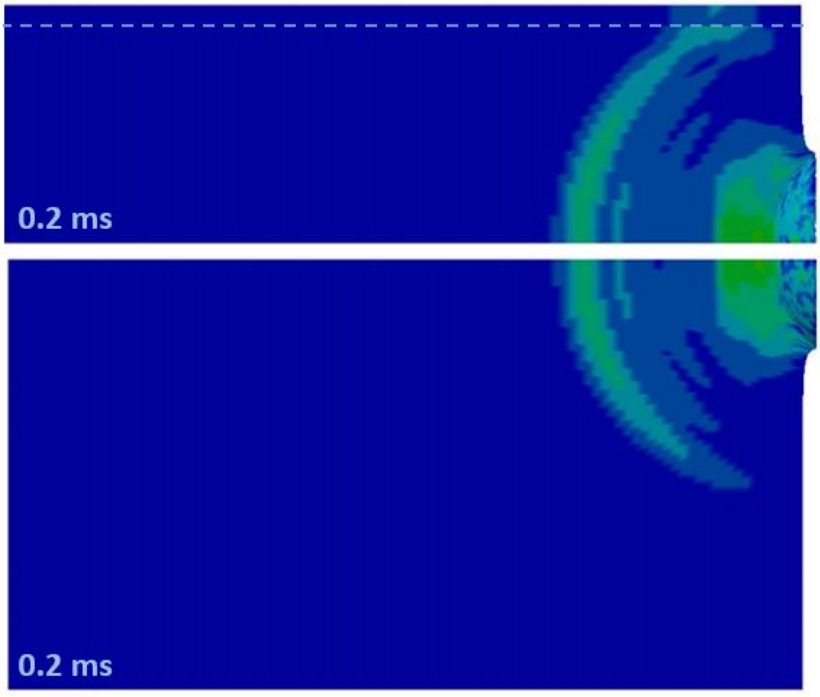

Fig. 22 Pressure contours at 0.2 ms for rectangular and cylindrical setup

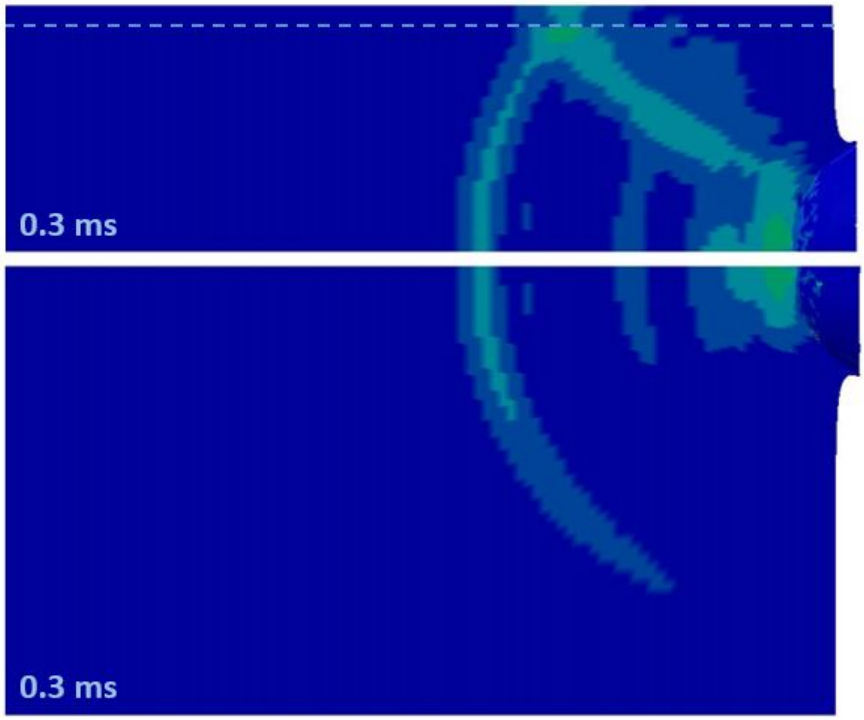

Fig. 23 Pressure contours at 0.3 ms for rectangular and cylindrical setup

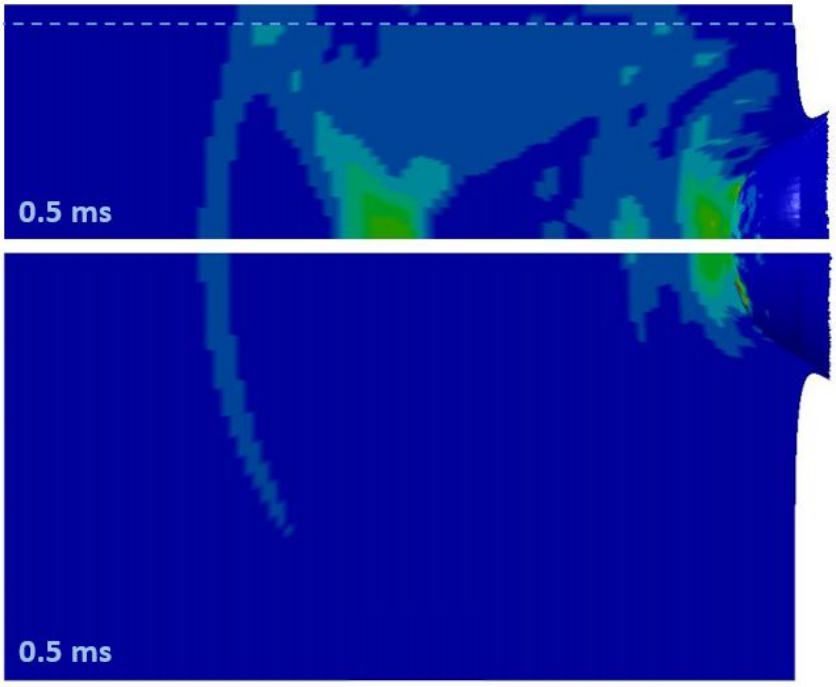

Fig. 24 Pressure contours at 0.5 ms for rectangular and cylindrical setup

The pressure contours in Fig. 21 are the same in the central region of the clay and radially outward. This is expected because the computational mesh is the same for both configurations to 3.0 inches in the clay, and the incident wave has not reached the PVC.

Figure 22 shows the pressure contours at 0.2 ms. They are the same for both configurations in the central region and radially outward to approximately 2.8 inches. At 2.0 ms the incident wave of the cylindrical setup has reached the clay–PVC boundary, been transmitted into the PVC, and is reflected back into the clay.

At 0.3 ms the leading wave continues in the direction of the penetrator for both geometries at the same magnitude and distance, located approximately halfway into the clay target shown in Fig. 23. The reflected wave in the clay of the cylindrical geometry has the same curved shape, but inward away from the PVC, as the incident wave traveling down the target; and the reflected wave has reached the central region, including the crater.

Figure 24 contains pressure contours at 0.5 ms. In the rectangular geometry, the initial pressure front continues toward the back of the target. In the cylindrical geometry, the initial pressure front is at the same location down the target as the rectangular setup, and there is significant wave interaction within the clay.

The presence of the PVC boundary has an effect on the dynamics within the clay and the formation of the crater. Figure 24 shows a region of higher pressure at the tip of the crater for the cylindrical case. The simulations demonstrate the PVC boundary influences the crater formation by approximately 0.25 ms, coinciding with the anticipated amount of time an incident wave and subsequent reflected wave would travel to the PVC boundary and back to the crater, respectively.

2.4 Drop-Test Results

2.4.1 Introduction

Prior to all BABT testing with clay backing material, column drop testing is performed to ascertain the readiness of RP#1 for impact and other testing. Figure 25 shows a schematic of a rectangular and cylindrical column drop test on the LHS and RHS, respectively. A 2.0-g steel dropper with hemispherical nose and cylindrical tail of equal radius, 0.875 inch (22.23 mm), is released, guided through a plastic column, 2.0 m from the strike face of a rectangular target and, separately, 2.0 m from the strike face of a cylindrical target. Measurements are taken of the DOP and must be between 22.0 and 28.0 mm in order to proceed to an impact test.[17]

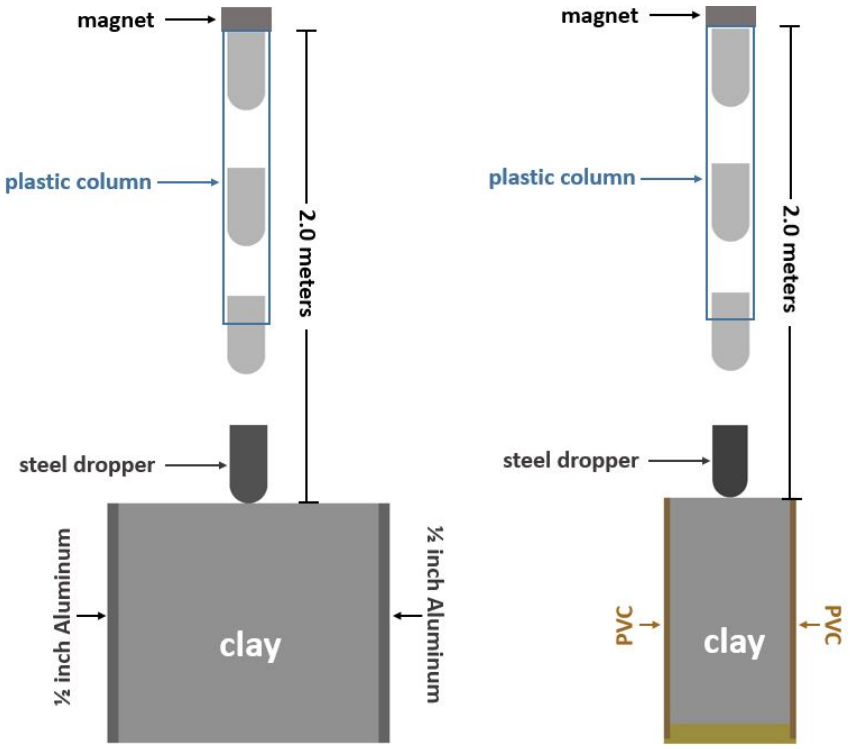

Fig. 25 Schematic of rectangular and cylindrical drop test

The computational mesh for the clay block and cylinder, the PVC, and wood are the same as in Fig. 8. However, the rectangular block of clay is confined on all sides by 0.5 inch (12.7 mm) of aluminum, noted in Fig. 26. A quarter problem is computed for each geometry due to symmetry, demonstrated in Fig. 26.

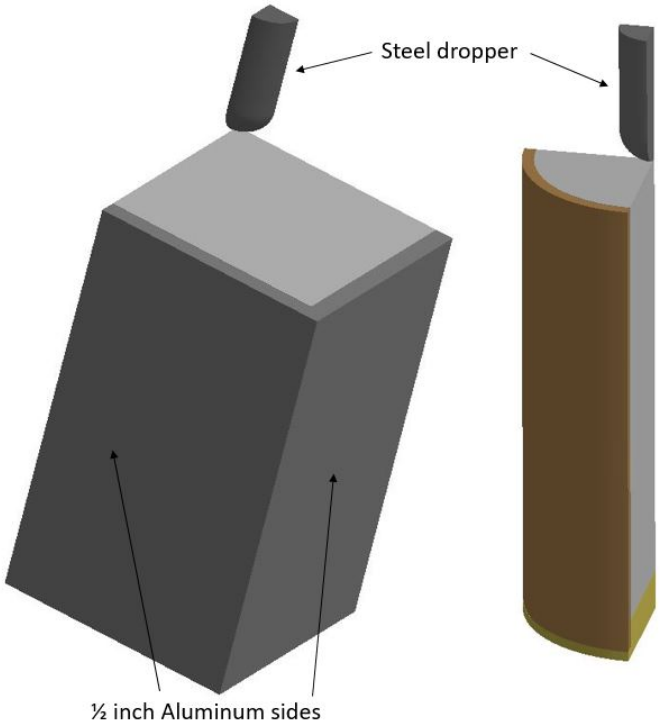

Fig. 26 Overhead rectangular and cylindrical strike face

The calculations were performed using LS-DYNA, as described in Section 2.2. The parameters for the steel dropper and aluminum are given in Table 3, shown in bold. The material model used for steel and aluminum are isotropic hypo-elastic (*MAT_ELASTIC). The clay model is the same as for reported for the impact tests.

Table 3 Material properties drop testing

Property	RP#1	Steel dropper	Aluminum sides	PVC	Wood
Density (kg/m^3)	1342	7700	2700	1375	600
Young's modulus (Pa)	15.0e6	1.9e11	6.9e10	2.5e9	7.0e9
Poisson ratio	0.49	0.30	0.33	0.40	0.40

The mesh for the cylinder and for the clay are the same as used in the drop tests, described in Section 2.2.2, and the boundary conditions between the clay and respective containers is an LS-DYNA sliding surface using the CF for the RP#1; that is, 0.19.

2.4.2 DOP

For the drop tests, all FE models were run with impact velocity 6.26 m/s, neglecting drag forces. The time history of the DOP for the cylindrical and rectangular configurations are given in Fig. 27 with blue and black curves, respectively. They are qualitatively the same; that is, both curves increase in magnitude to maximum DOP and stabilize.

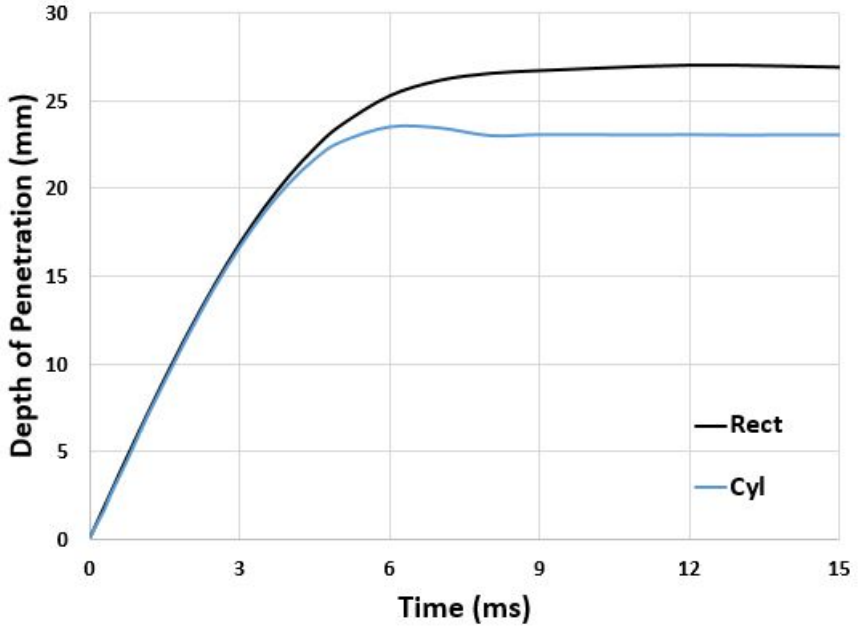

Fig. 27 Calculated drop-test DOP for cylinder and rectangle

The DOPs have the same values, from 0.0 ms to approximately 3.0 ms. Thereafter, the cylindrical DOP growth reaches its maximum value of 23.5 mm at approximately 6.0 ms and rebounds to approximately 23.0 mm, where it stabilizes; whereas for the rectangular geometry, the maximum DOP is approximately 26.5 ms attained at approximately 8.0 ms, after which the DOP stabilizes. The rectangular case does not experience rebound.

2.4.3 Clay Motion

Features of the motion of the clay drop test are similar to the side-impact dynamics; that is, there is an initial rapid rise to maximum DOP and stabilization. Craters form for both configurations but are not as pronounced. Clay is extruded from the PVC in the cylindrical case.

Side-by-side pressure contours for both geometries are given in Fig. 28 at 0.2, 0.3, and 0.4 ms, where the cylindrical case is on the LHS and the rectangular on the RHS; the dropper is not included in the figures. The vertical, dashed light-blue lines

on the left and right in each image mark the interface between the RP#1 and the PVC and aluminum sides, respectively. The pressure range is shown in the legend on the RHS in pascals, where the peak pressure is always in the central region at the tip of the dropper.

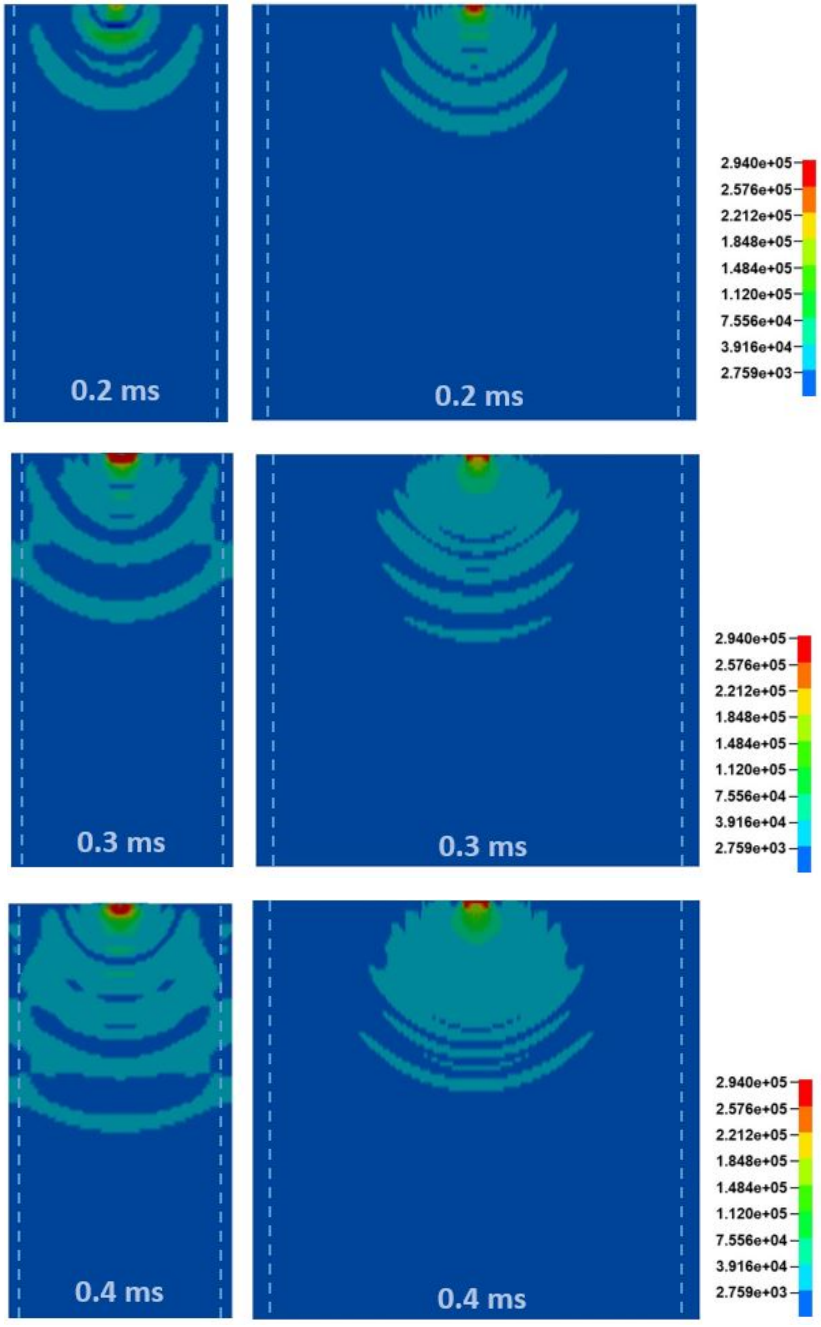

Fig. 28 Drop-test pressure contours, both configurations

At 0.2 ms, the pressure wave has almost reached the PVC–clay interface. In the rectangle's calculation the pressure wave is deeper than in the cylindrical case by approximately 0.12 inch due to the difference in the mesh (described in Section 2.3.3), including that all element lengths in the z-direction for the rectangular case are longer than in the cylindrical case, whereas the cylindrical elements are nearly square. At 0.3 ms, radially an inward rebound from the PVC coalesces with the central wave moving in the direction of the dropper and continues through 0.4 ms. In the rectangular calculation, from 0.2 to 0.4 ms, there is no influence from the aluminum–clay boundary.

For all drop-test simulations, the velocity is set at 6.26 m/s, neglecting drag force; however, there are drag forces and, in addition, during a drop-test series the plastic guide tube can collect debris on the inner diameter and possibly cause variation in the drop velocity and in the yaw of the dropper.

Drop-velocity variations were simulated at 5.80 m/s and 6.00 m/s, and a calculation was performed at 6.26 m/s with a 2° yaw. The results are shown in Fig. 29, where the green solid curve is 5.80 m/s, the solid red curve is 6.00 m/s, the dashed black curve is 6.26 m/s with 2° yaw in the dropper, and the original calculation at 6.26 m/s is the solid blue curve. The calculations show the maximum DOP for the rectangular geometry is 25.0–26.9 mm and for the cylindrical configuration is 22.1–23.5, which is 12%–13% less than the rectangular geometry.

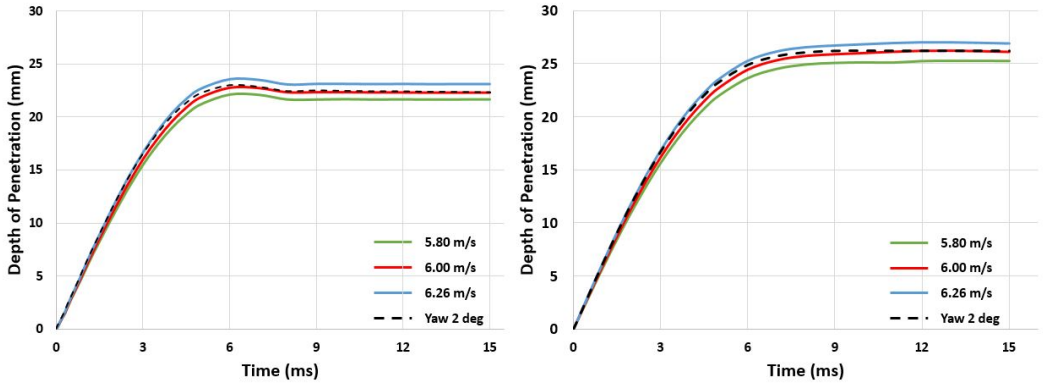

Fig. 29 Variations in velocity shown for drop tests, both geometries

Figure 30 shows maximum DOP versus velocity, where the dark-gray circles represent the rectangular geometry and the blue circles are for the cylindrical configuration. The rate of increase for the rectangular case is linearly increasing, whereas there is no trend for the cylindrical configuration due to the effects of the PVC boundary.

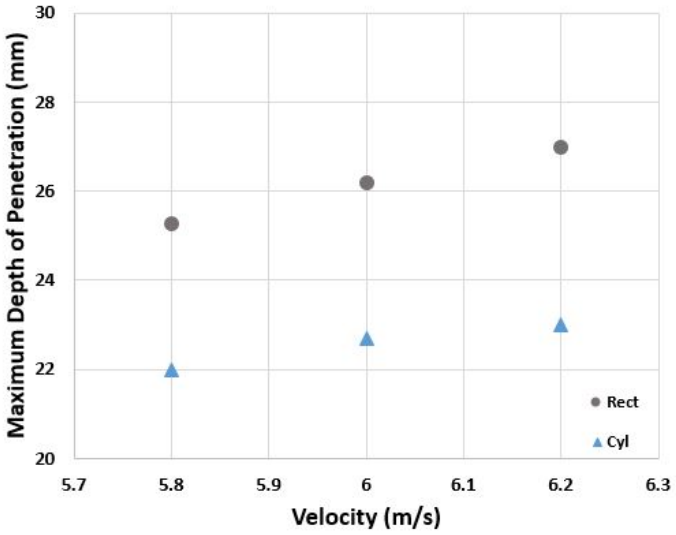

Fig. 30 Variations in velocity vs. maximum DOP in drop tests, both geometries

The cylindrical drop test is not a reliable test configuration that can be used to generate data to validate constitutive models for RP#1. Data from a drop test using a high-speed camera are only valid up to approximately 0.2 ms. A redesign for the cylindrical target will require increasing the radius and, as such, is not necessary since the rectangular geometry is sufficient, especially since the DOP is measured either by high-speed camera or FARO scanner.[29]

3. Summary and Conclusion

An historical background was presented for the evolution of backing material to study BABT leading to the current use of RP#1. The traditional rectangular clay target was modified to accommodate advances in data collection by reducing the surface area of the clay strike face but retaining the length in the impact direction and confining the RP#1 within piping material.

Modernized experimental investigations of side-impact testing and drop testing indicate the piping material and reduced surface strike-face area influences the dynamics of the DOP and the formation of the crater within the backing material.

The modeling and analysis demonstrated that confining the backing material and reducing the strike-face surface area reduces the magnitude of the maximum DOP for impact testing and drop testing at all velocities tested. The magnitude of DOP for impact testing for cylindrical geometry was reduced by as much as 50%, depending on the clay–confining-material boundary conditions, and the magnitude of the DOP for drop testing was reduced by nearly 10% for the cylindrical setup.

The reduction in DOP is caused by reflected waves from the PVC, coupled with extruded clay along the boundary.

FE analysis of each geometry was performed for both side-impact testing and drop testing of RP#1, including analysis of mesh techniques and boundary conditions, variation of velocity and yaw, radial variation of the reduced target, and boundary-condition sensitivity to friction parameter; also, an in-depth investigation was made into the motion of the clay during penetration.

Numerical treatment of the clay–confining-material interface varied depending on friction parameters used. The DOP for an artificially high CF, 0.8, converges to a nonslip boundary condition, and those assigned to RP#1 and PVC increase toward the minimum DOP from Ivancik's Prather-type experiments. While higher coefficients of friction are used in practice, future numerical work must include formal sensitivity studies in conjunction with parameter sweeps in constitutive models to quantify friction effects, including whether they mask deficiencies within other models.

The numerical investigation demonstrated that after approximately 0.23 ms from initial contact of the penetrator with the clay target the DOP and crater formation in the cylindrical configuration are influenced by the boundary.

4. References

1. Lehowicz L. Phase III report on review of the testing of body armor materials for use by the US Army. Washington (DC): The National Academies; 2012.

2. Goldfarb M, Clurej T, Weinstein M, Metker L. A method for soft body armor evaluation: medical assessment. Aberdeen Proving Ground (MD): Edgewood Arsenal (US); 1975. Report No.: EB-TR-74073.

3. Clare V, Lewis J, Mickiewicz A, Sturdivan L. Blunt trauma data correlation. Aberdeen Proving Ground (MD): Edgewood Arsenal (US); 1975. Report No.: EB-TR-75016.

4. Soderstrom C, Carroll A, Hawkins C. The medical assessment of a new soft body armor. Aberdeen Proving Ground (MD): Chemical Systems Laboratory (US); 1977. Report No. ARCSL-TR-77057.

5. Nicholas N, Welsch J. Ballistic gelatin. University Park (PA): Institute for Non-Lethal Defense Technologies, Pennsylvania State University; 2004 Feb.

6. Prather R, Swann C, Hawkins C. Backface signatures of soft body armors and the associated trauma effects. Aberdeen Proving Ground (MD): Edgewood Arsenal (US); 1977. Report No.: ARCSL-TR-7705.

7. Metker L, Prather R, Johnson E. A method for determining backface signatures of soft body armors. Aberdeen Proving Ground (MD): Edgewood Arsenal (US); 1975 May. Report No.: EB-TR-75029.

8. Ivancik J, Havard R, Mrozek R. Penetration profiles of ballistic backing materials for body armor testing. Aberdeen Proving Ground (MD): Army Research Laboratory (US); June 2017. Report No.: ARL-TR-8049.

9. Schuster B, Jannotti P, Debonis, D. Unpublished results from Activity 4.1—experimental study of the dynamics of hard armor and ballistic clay. Aberdeen Proving Ground (MD): Army Research Laboratory (US); 2018 May.

10. van der Jagt-Deutekom M, Carton E, Philippens M. Separation phenomena between armour plate and clay backing during projectile impact. Netherlands Organisation for Applied Scientific Research (TNO); 2012 Oct. Report No.: 2012 R10755.

11. Bir C, Lance R, Stojsih-Sherman S, Cavanaugh J. Behind armor blunt trauma: Recreation of field cases for the assessment of backface signature testing. In: Chocron S and Walker J, editors. Ballistics 2017. Proceedings of 30th

International Symposium on Ballistics; 2017 Sep 11–15; Long Beach, CA. Lancaster (PA): DEStech Publications; 2017.

12. Green AP. XLII. The use of plasticine models to simulate the plastic flow of metals. London, Edinburgh, Dublin Phil Mag J Sci. 1951;42(327):365–373.

13. Sofuoglu H, Rasty J. Flow behavior of plasticine used in physical modeling of metal forming process. Tribology Int. 2000;33:523–529.

14. Altan T, Hennings H, Sabroff A. The use of model materials in predicting forming loads in metal working. J Manuf Sci Eng. 1970;92(2):444–451.

15. Eckerson K, Liechty B, Sorensen C. Thermomechanical similarity between materials in predicting forming loads in metal working. J Strain Anal Eng Des. 2008;43(5):383–394

16. Azevedo R, Alves M. Numerical simulation of soft-body impact on GFRP laminate composites: mixed SPH-FE and pure SPH approaches. Mech Solids Braz. 2009:15–30.

17. Test Operating Procedure 110-2-210. Ballistic testing of hard body armor using clay backing. Aberdeen Proving Ground (MD): Aberdeen Test Center (US); 2008 Jan.

18. NIJ Standard–0101.06. Ballistic resistance of body armor. Washington (DC): National Institute of Justice, Department of Justice (US); 2008 Jul.

19. Hernandez C, Buchely M, Maranon A. Dynamic characterization of Roma Plastilina no. 1 from drop test and inverse analysis. Int J Mech Sci. 2015;100:158–168.

20. Raybek D. Finite element simulations of drop indentations into oily clay. Norwegian Defence Research Establishment (FFI); 2015 Jan. Report No.: 2014/02221.

21. Zhang T, Ivancik J, Mrozek A, Satapathy S. Material characterization of ballistic Roma Plastilina no. 1 clay. In: Chocron S and Walker J, editors. Ballistics 2017. Proceedings of 30th International Symposium on Ballistics; 2017 Sep 11–15; Long Beach, CA. Lancaster (PA): DEStech Publications; 2017.

22. LS-DYNA. Livermore (CA): Livermore Software Technology Corporation; 2019 [accessed 2019 Aug 21]. http://www.lstc.com/products/ls-dyna.

23. Bojanowski C, Kulak RF. Comparison of Lagrangian, SPH and MM-ALE approaches for modeling large deformation in soil. In: 11th International LS-DYNA Users Conference; 2010; Detroit, MI. p. 45–56.

24. Erhart T. Review of solid element formations in LS-DYNA: properties, limits, advantages, disadvantages. Presentation at LS-DYNA Forum; 2011 Oct 12; Stuttgart, Germany.

25. PVC pressure pipe. Sydney, Australia: Vinidex; 2019 [accessed 2019 Aug 21]. www.vinidex.com.au/technical/material-properties/pvc-properties.

26. Densities of wood species. Engineering ToolBox; 2004 [accessed 2019 Aug 21]. www.engineeringtoolbox.com/wood-density-d_40.html.

27. Snyder E. Weapons and Materials Research Directorate, Aberdeen Proving Ground (MD). Personal communication, 2018 July.

28. Oelze M, Darmody R, O'Brien W. Measurement of attenuation and speed of sound in soils for the purposes of imaging buried objects. J Acous Soc America. 2001;109(5):2287.

29. Portable 3D measurement arms. FARO Technologies, Inc.; 2019 [accessed 2019 Aug 21]. https://www.faro.com/products/3d-manufacturing/faroarm/.

List of Symbols, Abbreviations, and Acronyms

BABT	behind-armor blunt trauma
BFD	back face deformation
CF	coefficient of friction
DOP	depth of penetration
FE	finite element
HIDRA	High Voltage In-situ Diagnostic Radiography Apparatus
LHS	left-hand side
LTSC	Livermore Technology Software Corporation
MM-ALE	Multi-Material Arbitrary Lagrangian-Eulerian
PPE	Personal Protective Equipment
PVC	polyvinyl chloride
RHS	right-hand side
RP#1	Roma Plastilina No. 1
SPH	Smoothed Particle Hydrodynamic
TNO	Netherlands Organization for Applied Scientific Research
TOP	Test Operating Procedure

1 (PDF) DEFENSE TECHNICAL INFORMATION CTR DTIC OCA

2 (PDF) CCDC ARL FCDD RLD CL TECH LIB

1 (PDF) GOVT PRINTG OFC A MALHOTRA

13 (PDF) NATICK SOLDIER RSRCH DEV AND ENGRNG CTR M G CARBONI M CODEGA D COLANTO R DILALLA B FASEL J FONTECCHIO B KIMBALL J KIREJCZYK M MAFEO M MARKEY J PARKER D PHELPS J WARD

3 (PDF) PROG EXECUTIVE OFC SOLDIER A FOURNIER J MULLENIX E BEAUDOIN

1 (PDF) AUTO CELL PEO LAND SYS A PURTELL

2 (PDF) OFFICE OF NAVAL RESEARCH T BENTLEY K YANKASKAS

1 (PDF) NAVAIR PATUXENT RIVER B SHENDAR

1 (PDF) INST FOR DEFNS ANLYS Y MACHERET

4 (PDF) MRMC DOD BLAST INJURY RSRCH PROG COORDINATING OFC R GUPTA M LEGGIERI R SHOGE S HINDS

3 (PDF) MRMC JTAPIC PRGM OFC F LEBEDA W LEI J USCILOWICZ

4 (PDF) US ARMY AEROMEDICAL RSRCH LAB F BROZOSKI V CHANCEY B MCENTYRE D WISE

1 (PDF) TARDEC R SCHERER

1 (PDF) RDECOM HQ AMSRD PE D RUSIN

1 (PDF) EDGEWOOD CHEML AND BIOL RSRCH DEV AND ENG CTR M HORSMON

1 (PDF) OSD DOT&E J IVANCIK

48 (PDF) ARL
FCDD DAS L
P BAKER
T STADTERMAN
P DISALVO
N EBERIUS
N ELDREDGE
FCDD DAS LC
M PERRY
FCDD DAS LBE
J GURGANUS
M COHEY
S COARD
FCDD DAS LBG
M ROTHWELL
F REYNOLDS
FCDD DAS LBS
R DIBELKA
FCDD DAS LBW
G DIETRICH
M ENDERLEIN
A KULAGA
K LOFTIS
W MERMAGEN
S SNEAD
R VANAMBURG
FCDD RLW
S SCHOENFELD
FCDD RLW B
C HOPPEL
FCDD RLW L
A DAGRO
A DILEONARDI

A EIDSMORE
FCDD RLW LC
T PIEHLER
FCDD RLW P
R FRANCART
FCDD RLW PA
S BILYK
FCDD RLW PB
S ALEXANDER
T BAUMER
A BROWN
B FAGAN
M GRAHAM
A GUNNARSSON
C HAMPTON
M KLEINBERGER
E MATHEIS
J MCDONALD
P MCKEE
K RAFAELS
S SATAPATHY
K WEAVER
T WEERASOORIYA
S WOZNIAK
T ZHANG
FCDD RLW PC
M FERMEN-COKER
FCDD RLW PD
J RUNYEON
FCDD RLW PE
P SWOBODA
FCDD RLW PG
N GNIAZDOWSKI